Chapter 14
Kinetic Monte Carlo Modeling of Nanomechanics in Amorphous Systems

Eric R. Homer, Lin Li, and Christopher A. Schuh

14.1 Introduction

Modeling the nanomechanics of amorphous systems presents a unique challenge as a result of the disparate time and length scales and diverse modes of deformation exhibited by this class of materials [1, 2]. At high temperatures, amorphous systems exhibit homogeneous deformation that follows Newtonian and non-Newtonian flow laws. At low temperatures, deformation is localized into shear bands with nanometer scale thickness but which can extend over hundreds of micrometers. Interestingly, a single fundamental unit of deformation is hypothesized to underlie these diverse modes of deformation. This fundamental unit of deformation is known as the shear transformation zone or STZ, and is characterized by the transient motion of several dozen atoms that deform inelastically in response to an applied shear stress [3]. The STZ is illustrated in Fig. 14.1 where the final state has been sheared by an increment of shear strain γ_o. The two modes of deformation are then expected to be comprised of either the uncorrelated activation of STZs uniformly distributed throughout the sample—in the case of homogeneous deformation—or of highly correlated activation of STZs in a localized band—in the case of inhomogeneous deformation [4].

E.R. Homer (✉)
Department of Mechanical Engineering, Brigham Young University, Provo, UT 84602, USA
e-mail: eric.homer@byu.edu

L. Li
Department of Metallurgical and Materials Engineering, University of Alabama, Tuscaloosa, AL 35487, USA

C.A. Schuh
Department of Materials Science and Engineering, Massachusetts Institute of Technology, Cambridge, MA 02139, USA

C.R. Weinberger, G.J. Tucker (eds.), *Multiscale Materials Modeling for Nanomechanics*, Springer Series in Materials Science 245,
DOI 10.1007/978-3-319-33480-6_14

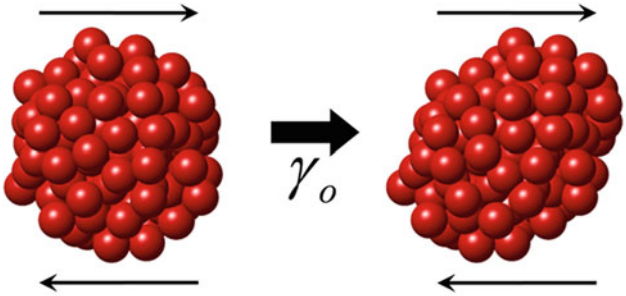

Fig. 14.1 Shear transformation zone (STZ), which represents the response of a collection of atoms to an applied shear stress. The final state of the atoms has been sheared from the initial state by a plastic strain of γ_o. Figure adapted with permission from [29]

Modeling this behavior is difficult because STZ activations in these cases can occur over several decades of strain rate. Furthermore, simultaneously capturing the length scale of nanometer shear band thickness and micrometer shear band slip is challenging. To truly resolve the nature of deformation within these materials, the mechanics must be modeled using a combination of modeling approaches [2]. Atomistic simulations are critical in resolving the mechanics associated with individual STZ activations as well the nature of STZ–STZ interactions [5, 6]. Unfortunately, the time and length scale limitations of atomistic simulations preclude simulating the behaviors of these materials at engineering time and length scales [2]. Continuum approaches, on the other hand, provide the ability to model deformation at engineering scales and provide ideal comparison to experiments [7–10]. However, the continuum approach is limited by its constitutive laws, which are often changed to accommodate the different modes of deformation [8, 9]. This can lead to the possibility of incorrectly capturing the deformation physics. As a result, modeling the behavior across the entire spectrum is best enabled by the addition of an intermediate or mesoscale technique [2]. Mesoscale techniques focus on capturing the physics that bridge the time and length scales between atomistic and continuum methods [11].

14.2 Mesoscale Modeling

The key to a mesoscale modeling technique that successfully bridges the time and length scales of interest is to adopt elements that accurately capture the physics associated with the fundamental events. In the mesoscale model adopted here, we employ two separate elements that individually bridge the time and length scales associated with deformation in amorphous systems. The kinetic Monte Carlo (kMC)

algorithm is adopted to bridge the time scales, while a coarse-graining technique is utilized to bridge the length scales. It is noted, however, that there are a variety of mesoscale approaches that can be adopted [11, 12].

14.2.1 Coarse-Graining

The technique of coarse-graining involves the identification of features of a given process such as a cluster of atoms, an entire crystal of atoms, or region of material, and then treating the cluster, crystal, or region as a single unit. Atomic interactions, vibrations, defects, molecular interactions, and various other phenomena that do not play a governing role in the process of interest can either be ignored or their contributions can be incorporated into the constitutive law that governs the coarse-grained region. For example, polymer or protein modeling often treats the molecules or different clusters of atoms as different individual units [12]. This is efficient because the individual atomic interactions no longer need to be considered, and the net interaction between the clusters of atoms can be accommodated with a constitutive law. The result of coarse-graining is that one can model larger systems sizes more efficiently while ensuring that there is little loss in accurate physical interactions between the coarse-grained regions.

14.2.2 The kMC Algorithm

The kMC algorithm is an adaptation of the well-known Monte Carlo technique. The Monte Carlo technique uses probability distribution functions to sample the phase space of systems in equilibrium states. That is, in these algorithms, a system is examined for many different equilibrium configurations it can adopt and the system is moved into states that have higher probability of existence based on the equilibrium energy. The probability distribution most frequently used is the Maxwell–Boltzmann distribution

$$p\left(E_i\right) = \exp\left(-E_i/k_B T\right)/\Omega \tag{14.1}$$

where E_i is the energy of the system in configuration i, k_B is Boltzmann's constant, T is the temperature in Kelvin, and Ω is the partition function, which is defined as

$$\Omega = \sum_i \exp\left(-E_i/k_B T\right). \tag{14.2}$$

In this definition, the probabilities of all the states sum to one.

Consider the following system with five possible configurations, whose energetic landscape is illustrated in Fig. 14.2. If the system starts in state 3 at low temperature,

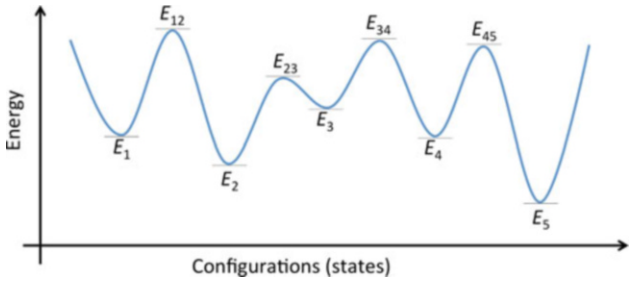

Fig. 14.2 Energetic landscape with various equilibrium states and transition states identified

it has the highest probability of visiting state 5, although it will visit all states according to the probabilities calculated by Eq. (14.1). Whether a different state can be accessed is dependent only on the change in energy between the equilibrium states, and the magnitude of the energy barrier separating the two states is irrelevant. MC algorithms can even transition to states that are not adjacent (state 1 directly to state 5) and time is not accounted for because the time to overcome the transition state barriers is not considered.

The kMC algorithm on the other hand is focused on the energy barriers and transition states between individual states and tracks time evolution during this process. The algorithm and the underlying transition state theory (TST) are explained in detail by Voter in [13]. According to TST, a system can only transition into adjacent states. The probability for transitioning between states is now based on the energetic difference between the current equilibrium state and transition state between the adjacent states. For a transition from state i to state j, this energetic barrier works out to

$$\Delta E_{i\to j} = \Delta E_{ij} = E_{ij} - E_i \tag{14.3}$$

The transition rate k from state i to j is then given by the Arrhenius equation:

$$k_{ij} = \nu \ \exp\left(-\Delta E_{ij}/k_B T\right) \tag{14.4}$$

where ν is the attempt frequency of the system to transition out of a given state. For most atomic processes, ν is related to the Debye frequency for the elements involved. It is assumed that once the system moves from the equilibrium state to the transition state, it will continue along its trajectory into the new equilibrium state.

As an example, consider again the system in Fig. 14.2, with the system starting in state 3. Since the system can only transition from state 3 into state 2 or 4, the two probabilities will be based on the energetic differences ΔE_{32} and ΔE_{34}. Since ΔE_{32} is smaller, the system is more likely to transition into state 2 than state 4. Going further, getting to state 5 is less likely than getting to state 2 because the two transitions required to get to state 5, ΔE_{34} and then ΔE_{45}, are so much larger than

the single transition required to get to state 2, ΔE_{23}. This contrasts the MC results that would suggest state 5 as the most likely state to be occupied. However, with sufficient time and/or thermal energy, the kMC algorithm can and will visit state 5.

The kMC algorithm proceeds according to the following steps [14], which are repeated for every transition:

1. Make a list of transition states, enumerated by the index j, out of the current equilibrium state and calculate the rate for every transition k_j. (Note that the current equilibrium state is no longer listed as a subscript in this derivation.) Calculate the cumulative transition rate k_T and normalize each individual transition $\eta_j = k_j/k_T$, such that the sum over the normalized transitions, η_j, is equal to one.
2. Generate two random numbers, ξ_1 and ξ_2, uniformly on the interval (0,1].
3. Update the elapsed time of the simulation with the residence time in the current configuration, calculated according to

$$\Delta t = -\ln\ \xi_1/k_T \tag{14.5}$$

4. Select a single transition to implement by first calculating the partial cumulative rate according to

$$H_j = \sum_{n=1}^{j} \eta_n \tag{14.6}$$

   and then use the random number, ξ_2, to find the single transition i to implement, which satisfies

$$H_{i-1} < \xi_2 \leq H_i. \tag{14.7}$$

   Note that when the transition events are listed in a successive fashion, ξ_2 falls in the subinterval η_i in the list of normalized rates.
5. Move the system into the new state by implementing the transition selected in the previous step.
6. Update any system calculations and return to step 1 to allow the system to evolve again.

The kMC algorithm repeats the steps above for any desired number of transitions, and allows the system to evolve by passing through transitions based on their probability for occurring and tracking the elapsed time between transitions. The kMC algorithm is powerful and has been used in numerous studies to investigate diverse phenomena [15–21].

One important aspect of the kMC algorithm and TST is that detailed balance must be obeyed. Essentially, detailed balance ensures that one is accurately sampling the phase space of possible equilibrium states and their transition pathways for microscopic reversibility. By definition, all processes at equilibrium must be balanced. Voter [13] explains detailed balance as:

> For every pair of connected states i and j, the number of transitions per unit time (on average) from i to j must equal the number of transitions per unit time from j to i. Because the number of escapes per time from i to j is proportional to the population of state i [based on MC probability of population] times the rate constant for escape from i to j, we have $p(E_i) \cdot k_{ij} = p(E_j) \cdot k_{ji}$ and the system is said to "obey detailed balance."

This can also be viewed as ensuring that the energetic landscape between states i and j be identical whether the system is transitioning from i to j or from j to i [4]. Additional discussion of detailed balance is available in referenced works [13, 22].

The kMC algorithm will provide an accurate model of a physical system so long as the transition states available to the algorithm accurately model the actual transition states of the physical system. A complete description of the kMC algorithm and many features and requirements of the technique are discussed in detail by Voter [13].

14.3 STZ Dynamics

To simulate the nanomechanics of amorphous systems, a mesoscale STZ dynamics modeling framework has been developed. This framework is inspired by the work of Bulatov and Argon [23–25], but extends the work in several ways. The method centers on the STZ introduced in Sect. 14.1. Since the cluster of atoms in an STZ consistently exhibit a transient shearing motion [5, 6, 26–28], it is possible to coarse-grain a theoretical sample into a system of potential STZs. Then each potential STZ has the ability to shear in the same manner as a cluster of atoms. This coarse-graining enables more efficient sampling of larger system sizes, thereby fulfilling one of the two improvements to modeling amorphous systems.

The second aspect of the STZ dynamics framework involves simulating longer system times more efficiently. This is accomplished by considering the transient STZ activation as a transition state between the initial and final equilibrium configurations. Thus, TST and the kMC algorithm can be employed as long as knowledge of the energetic landscape, including the transition states, is available.

14.3.1 STZ Coarse-Graining

In the present work, coarse-graining is accomplished by replacing the cluster of atoms that represent a potential STZ with features of a finite element mesh. In the development of the STZ dynamics framework, three criteria were identified as critical to proper representation of an STZ using a finite element mesh [14, 29]. First, the coarse-grained representation should approximate the shape of an STZ, which is generally believed to be roughly spherical. Second, since the STZ is a transient event, the definition of any potential STZs should enable them to overlap. The reason for this is that atoms would never be restricted to participate in only

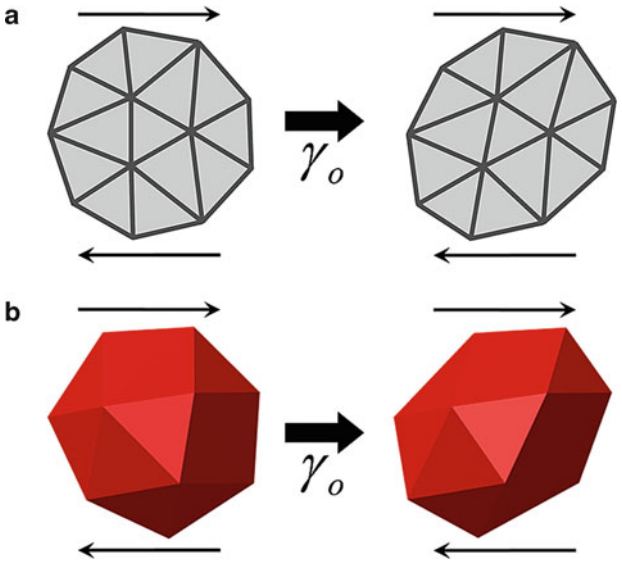

Fig. 14.3 Coarse-graining of an STZ using features of a finite element mesh in (**a**) 2D and (**b**) 3D. Figures adapted with permission from [14, 29]

one potential STZ. By defining them in a way that they overlap, any given element, which represents smaller groups of atoms, can participate in multiple potential STZ activations. Third, the coarse-grained STZ should accurately capture the expected behavior of an STZ. In his original proposal of the STZ, Argon modeled the STZ as an Eshelby inclusion [3]. As a result, analytical solutions can be utilized as a reference against which to compare a given coarse-graining technique and ascertain its accuracy [30, 31].

Following these criteria, techniques for coarse-graining STZs onto 2D and 3D finite element meshes were identified. In 2D, the technique involves the identification of a node and all surrounding elements or an element and all surrounding elements to represent a single STZ. This is illustrated in Fig. 14.3a for a 2D mesh that shows an element-centered, coarse-grained STZ. In 3D, a node and all surrounding elements are used to represent a single STZ, which is illustrated in Fig. 14.3b. These coarse-graining techniques have been shown to satisfy the three criteria stated above. Namely, the shapes are roughly equiaxed, potential STZs overlap, and as shown in published work, the error between the finite element solution and Eshelby inclusions solution is small [14, 29].

The use of finite elements builds on the previous work by Bulatov and Argon in an important way. In their original work, Bulatov and Argon employed a rigid lattice STZ model, which could track stress and strain but not displacement [23]. In the STZ dynamics modeling framework, the finite element mesh enables the framework to track displacement and deformation in addition to stress and strain. Additionally,

the lattice model did not allow STZs to overlap, whereas the finite element mesh does allow this.

14.3.2 kMC Implementation

The implementation of the kMC algorithm in the STZ dynamics framework follows all the steps defined in Sect. 14.2.2 with one important addition. In selecting a single event, one must not only pick the STZ that will shear but also the direction of shear. In the original 2D model of Bulatov and Argon, each potential STZ had the ability to shear in one of six directions [23]. This simplified the number of transition events that had to be considered for each iteration of the kMC algorithm. However, just as atoms are not restricted to participate in only one possible STZ event, STZs are not restricted to shear in only six possible directions. In 2D, an STZ should be able to shear in any direction in a plane. In 3D, an STZ should be able to shear in any unique combination of shear planes and shear directions within that plane.

While it is relatively trivial to shear an STZ in any direction, enumerating and calculating the transition rates for all these directions is more challenging. We first begin with the calculation of the rate for an STZ to shear in one direction. The STZ activation rate is defined as

$$\dot{s} = v_o \ \exp\left(-\frac{\Delta G}{k_B T}\right) \tag{14.8}$$

where the prefactor v_o is of the order of the Debye frequency, ΔG is the activation energy barrier, and $k_B T$ is the thermal energy of the system.

In order to calculate the activation energy barrier for a given transition, one must have knowledge of the transition itself. Methods such as the nudged-elastic band [32] or the activation–relaxation technique [33, 34] can be used in atomistic simulations to find the exact activation energy barrier from any given equilibrium state. One can then use Monte Carlo techniques to evolve the system as in [35]. However, these atomistic energy barrier search methods are computationally intensive and do not readily translate to mesoscale models. Since we desire to have a catalog with a large number of transitions, we favor another approach.

More traditional approaches to determining the energy in mesoscale systems will follow three steps: (1) calculate the energy, E_I, at the initial equilibrium state, (2) move the system to and calculate the energy, E_F, in the final state, and (3) add a predefined barrier height, ΔF, to the intermediate energy, which is the average energy of the initial and final equilibrium states. This is illustrated in Fig. 14.4a, b. Unfortunately, this approach is time consuming because one must move the system to all of the possible final equilibrium states in order to calculate the transition state.

In their model, Bulatov and Argon [23] exploited the fact that the Eshelby approach results in a quadratic solution to the strain energy for shearing an STZ, illustrated in Fig. 14.4 as a dashed line. This quadratic solution can be used to

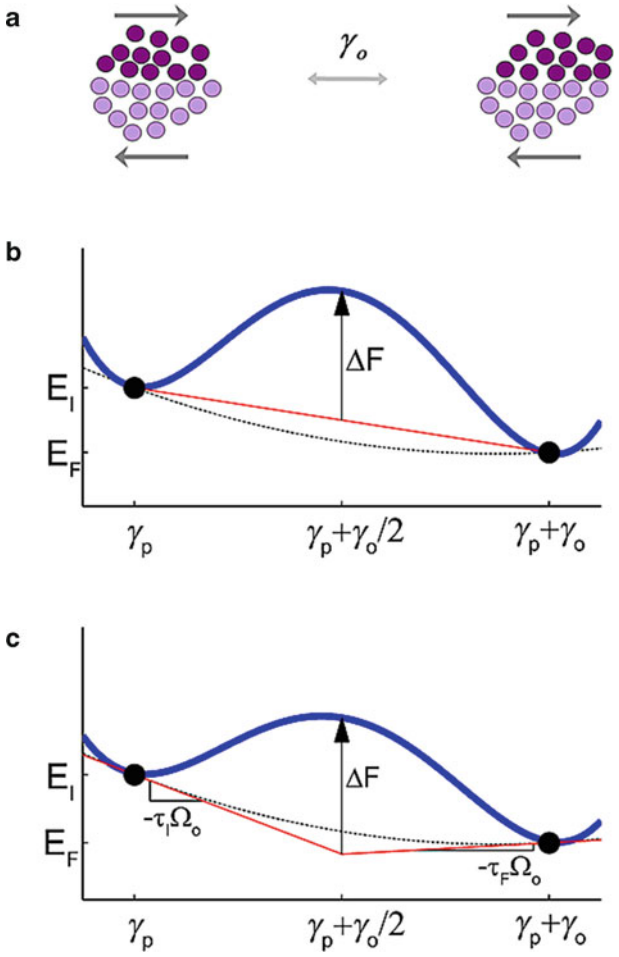

Fig. 14.4 (**a**) Representation of the two states before and after the activation of an STZ. Illustration of the energy landscape and the method of identifying the activated state of an STZ in a (**b**) traditional kMC model where the activation energy, ΔG, is obtained by adding the fixed energy barrier ΔF to the average of the initial and final states and (**c**) the energy landscape for the model proposed by Bulatov and Argon [23] where ΔG is obtained by adding ΔF to the projection of the slope (equal to the local shear stress) at the initial and final states. The variation in energy between the two states is given by *dashed line* and is the same in both (**b**) and (**c**). Figure reproduced with permission from [4]

predict the energy in the final state, but rather than calculate that final state energy, Bulatov and Argon simply extrapolate from the initial state, using the slope at that point, to the midpoint of the transition and then add the fixed barrier height, ΔF. Figure 14.4 accentuates the energy difference between the traditional approach and that of Bulatov and Argon for pedagogical purposes, but in actuality the difference in barrier height between the two methods is very small [4, 23]. Furthermore, the

method of Bulatov and Argon has the benefit of not having to calculate the energy of the final equilibrium state, which results in significant computational savings. A more detailed explanation of the calculations, including the important requirement of detailed balance, is discussed in [4].

Using the model of Bulatov and Argon, we can then define the activation energy barrier as

$$\Delta G = \Delta F - \frac{1}{2}\tau \cdot \gamma_o \cdot \Omega_o \tag{14.9}$$

where τ is the local shear stress and Ω_o is the volume of an STZ. Argon developed a model for ΔF [3], which is given as

$$\Delta F = \left[\frac{7-5\upsilon}{30\,(1-\upsilon)} - \frac{2\,(1+\upsilon)}{9\,(1-\upsilon)}\beta^2 + \frac{1}{2\gamma_o}\cdot\frac{\widehat{\tau}}{\mu(T)}\right]\cdot\mu(T)\cdot\gamma_o^2\cdot\Omega_o \tag{14.10}$$

where the three terms in the brackets define the strain energy associated with shearing of the STZ, the strain energy associated with a temporary dilatation of the STZ to allow the atoms to rearrange, and the frictional energy associated with the free shearing of the atoms over one another. In Eq. (14.10), υ is Poisson's ratio, β is a ratio of shear to dilatation (usually taken as 1), $\widehat{\tau}$ is the peak interatomic shear resistance between atoms, and $\mu(T)$ is the temperature-dependent shear modulus.

Since we are interested in calculating the range of barriers associated with shearing an STZ in any direction in 2D and 3D, the shear stress associated with each unique shear direction must be identified and enumerated.

14.3.2.1 STZ Activation Rate in 2D

In 2D, the shear stress for each unique shear direction around a circle can easily be evaluated using a Mohr's circle construct. Using this construct, the magnitude and sign of the shear stress along any given direction of the circle is equal to

$$\tau = \tau_{\max}\sin(\theta) \tag{14.11}$$

where θ is the angle to the stress state with stress τ, which is measured relative to the stress state with the highest principal stress. One can then integrate all shear directions by integrating θ over the interval [0°,360°). By combining Eqs. (14.8), (14.9), and (14.11), the integral STZ activation rate becomes

$$\dot{s} = \frac{v_o}{2\pi}\cdot\exp\left(-\frac{\Delta F}{k_B T}\right)\cdot\int_0^{2\pi}\exp\left(\frac{\tau_{\max}\cdot\sin(\theta)\cdot\gamma_o\cdot\Omega_o}{2k_B T}\right)\mathrm{d}\theta \tag{14.12}$$

which evaluates to a modified Bessel function of the first kind, of order zero

$$\dot{s} = \frac{v_o}{2\pi} \cdot \exp\left(-\frac{\Delta F}{k_B T}\right) \cdot I_o\left(\frac{\tau_{\max} \cdot \gamma_o \cdot \Omega_o}{2k_B T}\right). \tag{14.13}$$

This particular form of the STZ activation rate is convenient because the analytical solution gives the rate for shearing an STZ in any direction in two dimensions with only one function evaluation. This integral rate is evaluated for each STZ and utilized in the steps listed in Sect. 14.2.2. Upon selection of a given STZ for activation, the angle of shear is selected for that particular STZ by numerically evaluating the integral equation up to the fraction of overlap by the random number on that state. This angle selection is explained in more detail in [14]. Fortunately, the method can provide the STZ for activation and the angle of shear with the single random number ξ_2.

14.3.2.2 STZ Activation Rate in 3D

The evaluation of the STZ activation rate in 3D is more complex than the 2D case due to the larger set of possible shear planes and shear directions, as well as the need to only evaluate unique combinations of shear planes and directions. In a generalized form the integral activation rate can be defined as

$$\dot{s} = v_o \cdot \exp\left(-\frac{\Delta F}{k_B T}\right) \cdot \iiint_{g \in G} \exp\left(\frac{\tau\,(\sigma, g) \cdot \gamma_o \cdot \Omega_o}{2k_B T}\right) \mathrm{d}g \tag{14.14}$$

where g is the orientation of any shear plane–shear direction combination belonging to the set G of all unique combinations of shear planes and shear directions. The integral is three-dimensional because the specific orientation of a shear plane and shear direction requires three parameters. The shear stress of that orientation g is defined as $\tau(\sigma, g)$ to denote the fact that the triaxial stress state that exists in a given STZ must be transformed by g to obtain the shear stress for that given shear plane and shear direction. Due to the complexity of this calculation, the details are not discussed here but are available in [29]. In short, these details describe the process for defining all unique combinations of shear planes and directions, and note that no analytical solution to the integral in Eq. (14.14) could be found. However, interesting trends indicating the equation's sole dependence on the deviatoric stress, as well as symmetries in similar stress states, lead to an efficient solution. The integral is numerically evaluated and tabulated for rapid recall during the modeling process while maintaining an error less than 0.01 %.

In a similar fashion to the 2D case, the integral STZ activation rates are used to run the kMC algorithm and select an STZ for activation. Once again, the shear plane and direction for the selected STZ are chosen by numerically integrating the rate equation until the magnitude of overlap of the random number ξ_2 on the interval of the selected STZ is matched.

Table 14.1 Material properties commonly employed by the STZ dynamics framework

Property/variable	Symbol and value
Temperature-dependent shear modulus	$\mu(T) = -0.004\left[\text{GPa K}^{-1}\right] * T + 37\,[\text{GPa}]$
Poisson's ratio	$\nu = 0.352$
Debye temperature	$\theta_D = 327$ K
Fixed activation energy barrier	$\Delta F(T) = 0.822 \times 10^{-29}\left[\text{J Pa}^{-1}\right] * \mu(T)$
STZ volume	$\Omega_o = 2.0$ nm^3
STZ strain	$\gamma_o = 0.1$

14.3.3 Overall STZ Dynamics Framework

The STZ dynamics modeling approach incorporates the coarse-graining techniques and kMC algorithm evaluations of the STZ activation rates into an overall framework. The application of the framework to a given modeling problem requires that several steps be followed. First, a 2D or 3D finite element mesh is defined to match the geometry of the model material being simulated. Second, potential STZs are mapped onto the finite element mesh based on the technique determined according to the criteria discussed in Sect. 14.3.1. Third, the finite element mesh is assigned the set of material properties that will influence the material model and the kMC algorithm. In the present work, this limited set of properties is discussed in the following paragraph. Fourth, implement the kMC algorithm and repeat the following steps: (1) determine which STZ should be selected for activation, and which shearing angle should be applied, based on the current system state. (2) Apply plastic (Eigen) strains to the elements belonging to the STZ according to the selected shearing angle. (3) Use finite element analysis to determine the response of the system to the applied plastic strains. (4) Update the current system state, including stress, strain, and any functional material properties, to reflect the response to STZ activation. These last four steps involving the kMC algorithm are repeated many times in succession to determine the evolution of the system.

Due to the fact that the kMC algorithm determines and applies the plastic strains, the finite element analysis solver determines the elastic response of the system to the applied plastic strain, requiring only the use of a linear elastic solver.

The material properties and simulation variables used by many of the published STZ dynamics papers are listed in Table 14.1. This list is intentionally kept short to simplify the model and variables simply for the purpose of obtaining an intended response. The attempt frequency ν_o is taken as the Debye frequency, which can be calculated from the Debye temperature θ_D. The variables $\mu(T)$, ν, and θ_D are values for the commonly studied Vitreloy 1 with composition $Zr_{41.2}Ti_{13.8}Cu_{12.5}Ni_{10}Be_{22.5}$, and are obtained from [36], [36], and [37], respectively. Rather than using the complex form of the fixed barrier height in Eq. (14.10), we reduce ΔF to a simple functional form that is dependent upon the shear modulus. The STZ volume is in the range commonly reported in the literature [1, 38, 39] and the STZ strain is equal to the commonly accepted value [1].

14.3.4 Adaptations of the STZ Dynamics Framework

Since its original inception, the STZ dynamics framework has been adapted for different implementations and purposes.

First, the framework has been adapted for contact mechanics in finite element analysis to simulate nanoindentation [40]. In fact, the use of a finite element mesh and finite element analysis solver enables just about any set of boundary conditions regularly used in finite element analysis to be incorporated into the STZ dynamics framework.

Second, the kMC algorithm has been modified for specific scenarios to suppress the selection of a transition when that transition occurs on irrelevant time scales. This is crucial since standard kMC is designed to implement any transition selected by the algorithm no matter the elapsed time. Since stresses (and STZ activation rates) can vary by large magnitudes during nanoindentation or other testing conditions, this modified-kMC algorithm suppresses events that would occur on time scales greater than a predetermined maximum allowed time step. This ensures that stress and other conditions cannot change by a radical amount before being updated. In a given iteration, the modified-kMC algorithm determines the elapsed time before activating an STZ. If that elapsed time is larger than the maximum time, the STZ activation (plasticity) is suppressed and the system increments time by the maximum allowed time. If the elapsed time is smaller than the maximum time, the STZ activation (plasticity) is implemented and the system increments time by the amount suggested by the algorithm. In both cases, the elastic response of the system and all variables (stress, loading, displacement, etc.) are updated at the end of the step and the algorithm repeats with the updated values. In each iteration, an STZ may or may not activate, but the system can never evolve so rapidly that unphysical activations occur.

Third, state variables have been incorporated in some cases to account for the fact that the evolution of stress and strain cannot retain important information about the evolution of the structure. Free volume has been established as an important state variable for amorphous materials, so some implementations of the STZ dynamics framework track this state variable and adjust the material model to account for the current state of the structure at any given state.

Fourth, composite materials, such as metallic glass matrix (MGM) composites, have been simulated by partitioning the finite element mesh into two or more phases. Each element in the mesh is assigned a phase and the finite element solver uses the material model for that phase when that element is evaluated.

These various adaptations demonstrate the flexibility provided by the STZ dynamics framework, though other adaptations are certainly possible.

14.4 Applications of the STZ Dynamics Framework

Modeling amorphous materials using the kMC algorithm in the STZ dynamics framework provides an opportunity to study many different aspects of their nanomechanical behavior. In the following sections, we demonstrate: (1) how the framework can be used to study the various modes of deformation and understand the overall behavior of the model, (2) how thermomechanical processing can be investigated and how state variables are critical to capturing the evolution of the system, (3) how one can gain insight into the physics that control the nanomechanical behaviors of shear banding, (4) how mechanical contacts can be studied using the STZ dynamics modeling framework to gain insight into nanoindentation experiments on metallic glasses, and (5) how microstructural factors in MGM composites influence their mechanical properties.

14.4.1 General Behaviors

As noted in the introduction, amorphous materials exhibit homogeneous deformation at high temperatures and inhomogeneous deformation at low temperatures. To test the STZ dynamics framework, a model metallic glass with no preexisting distribution of stress and strain was subjected to two scenarios: high temperature (near Tg), intermediate stress and low temperature, high stress. Model responses for these two scenarios are shown in Fig. 14.5 for both 2D and 3D implementations. As can be seen, the first case exhibited the expected homogeneous deformation and STZs activated uniformly throughout the simulation cell. In the second case, the STZs localized the plastic strain into a shear band to give the expected inhomogeneous deformation.

Metallic glasses are expected to follow very specific rheological behaviors at higher temperatures. While the results are not shown here, both the 2D and 3D simulations closely follow the constitutive laws that are frequently used to fit experimental data.

To investigate the model responses over a range of conditions, we construct deformation maps for simulation cells subjected to a range of applied stresses at various temperatures. The deformation maps are illustrated for both 2D and 3D in Fig. 14.6. The steady-state strain rate is measured from each simulation and contours of constant strain rate are overlaid on the map for rates ranging form 10^{-10} to 1 s^{-1}. Simulations that had strain rates slower than 10^{-10} s^{-1} are deemed to be "elastic" and marked with an "×" as the deformation would be too slow to observe in experiments. Local values of the strain rate sensitivity are presented according to the shading inside each data point. As the stress is increased, the strain rate sensitivity decreases from unity (Newtonian flow), and trends toward zero (non-Newtonian flow). Finally, the regions of homogenous and inhomogeneous deformation are shaded. The 3D simulations are further broken down into shear banding versus

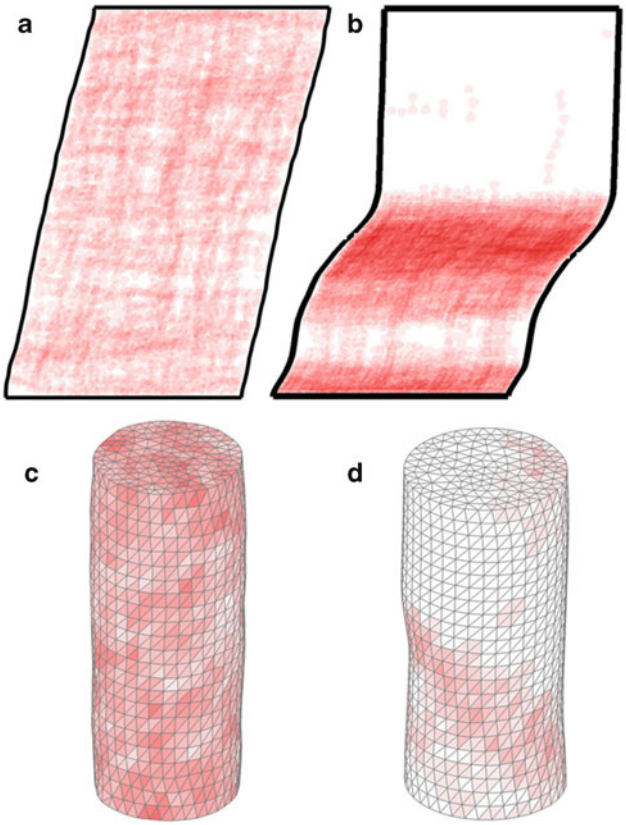

Fig. 14.5 High and low temperature representative responses of the STZ dynamics framework. The high temperature response is shown in (**a**) 2D and (**c**) 3D while the low temperature response is shown in (**b**) 2D and (**d**) 3D. Figures adapted with permission from [14, 29]

necking. This ability to distinguish between shear banding and necking is possible in the case of the 3D simulations because they were subjected to tension (3D) rather than pure shear (2D). These maps compare favorably with experimental deformation maps [1], in that they capture the basic features of amorphous deformation.

This match between experimental and simulated deformation maps is a testament to the strength of a mesoscale model that successfully coarse-grains a process and determines the transition states that control the evolution of the system.

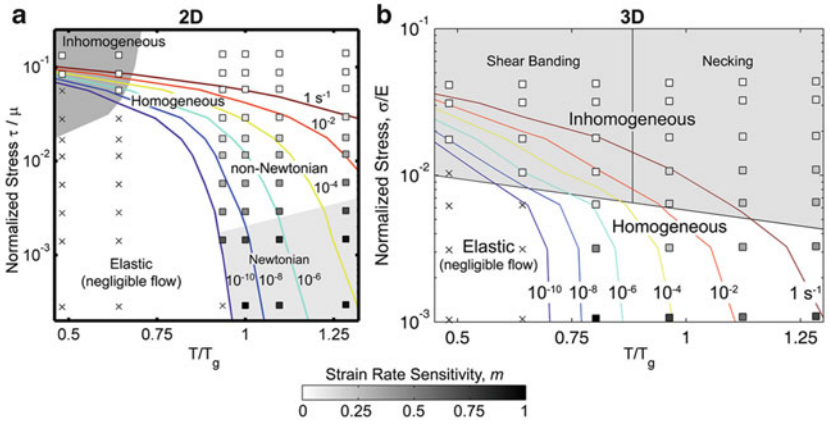

Fig. 14.6 Deformation maps for Vitreloy 1 constructed from data obtained by loading (**a**) 2D and (**b**) 3D model geometries over a range of loads and temperatures. The 2D simulations are subjected to pure shear while the 3D simulations are subjected to uniaxial tension. The *colored lines* represent contours of different steady-state strain rates, where strain rates slower than 10^{-10} s^{-1} are considered to be elastic and are marked with an "×." Other data points are shaded according to their respective strain rate sensitivity as indicated by the *color bar* below the map. Further regions marked as Newtonian (*lightly shaded*) and non-Newtonian are differentiated in the 2D map. The regions of homogeneous and inhomogeneous deformation are distinguished. In 3D this is further divided into samples which exhibit shear banding versus necking. Figures reproduced with permission from [14, 29]

14.4.2 Thermomechanical Processing and Free Volume

It is well known that the deformation behavior of an amorphous metal is sensitive to its processing history. Slowly quenched and well-annealed glasses show more serrated flow than quickly quenched glasses of the same composition [1, 2, 41]. As such, one desired capability of the STZ dynamics framework is to simulate thermomechanical processing and capture the effects of that processing history in subsequent deformation.

In the initial implementation of the STZ dynamics framework, processing history was captured only through the redistribution of stress and strain. As a result, when models with different processing history were tested, shear banding was not observed. The activation of STZs during thermal processing created a distribution of stress and strain whose magnitude was of the same order as the stress from an STZ activation attempting to form a shear band. As a result of this low signal-to-noise ratio, homogeneous deformation is observed even at low temperatures and high stresses in models that have been thermally processed [14].

To solve this problem, a state variable has been added to the STZ dynamics modeling framework [55]. The purpose of this state variable is to capture the evolution of the structure beyond the redistribution of stress and strain when an STZ is activated. One could choose from a range of state variables, such as atomic

stress and strains, topological or chemical order, etc., but the state variable of "free volume" has been widely adopted in such a way that it incorporates these effects indirectly [42–44].

In fact, in Argon's original definition of the STZ, he includes free volume as a state variable to capture the structural evolution of the system. In the free volume adaptation of the STZ dynamics framework, excess free volume, f_v, is defined as a normalized quantity where $f_v = 0$ corresponds to no excess free volume above the average polyhedral volume V^* in a dense random hard sphere glass, while $f_v = 1$ is an upper bound corresponding to a state where an STZ can be activated without accumulating extra free volume [2].

Since excess free volume influences the energy barrier for activation, the fixed barrier is redefined as

$$\Delta F_{\text{STZ}}(f_v) = \Delta F_{\text{shear}} + \Delta F_{v0} \cdot g_{\text{stz}}(f_v) \tag{14.15}$$

where ΔF_{shear} captures the strain energy associated with shear (not dependent upon excess free volume) and ΔF_{v0} captures the strain energy associated with dilatation and friction of the atoms sliding over each other (dependent upon excess free volume). Equation (14.15) essentially alters Eq. (14.10) by making the first term in the bracket of Eq. (14.10) equal to ΔF_{shear}, which is not dependent on the magnitude of excess free volume, and makes the last two terms in the bracket of Eq. (14.10) equal to ΔF_{v0}, since these are dependent upon the magnitude of excess free volume. In fact, ΔF_{v0} is smaller when greater excess free volume exists since the STZ will need to dilate less and the friction will be lowered. This change in the energy is captured by the function g_{stz}, which lowers the activation energy barrier as the excess free volume is increased.

Following a given STZ activation, the excess free volume within the activated STZ is increased since it is believed that the atoms are not able immediately return to the original magnitude of excess free volume.

In this model however, a competing process to the activation of STZs is introduced. This competing process is the diffusive rearrangement (and destruction) of excess free volume. As atoms are constantly vibrating, their thermal energy enables diffusive rearrangements that would enable a given region of material to lower its excess free volume. The rate of diffusive rearrangement is given as

$$\dot{s}_D = (1 - f_v)\, v_D \exp\left(-\frac{\Delta G_D(f_v)}{k_B T}\right) \tag{14.16}$$

where $\Delta G_D(f_v)$ is the activation energy barrier for diffusive rearrangement, which is dependent upon the current magnitude of excess free volume. Higher excess free volume has a lower energy barrier than lower excess free volume because it is farther from its equilibrium state. The quantity $(1 - f_v)$ reflects a decrease of available atomic sites for free volume diffusion as f_v increases. The prefactor v_D for the diffusive rearrangements is once again of the order of the Debye frequency.

In this free volume STZ dynamics framework, these diffusive rearrangement events are listed in the catalog of possible events. At any given kMC step, the system can activate an STZ or diffusely rearrange excess free volume. With this addition, the model retains information about its processing history beyond the simple redistribution of stress and strain.

The high temperature rheological behavior with the excess free volume state variable conforms to the Vogel–Fulcher–Tammann (VFT) relationship for viscosity. This is a nontrivial result because the model does not contain the input parameters to the VFT relationship; the behavior is an emergent result from the two competing processes.

At low temperatures, the excess free volume state variable enables the simulation to localize even in the presence of a preexisting stress and strain distribution. This can be seen in Fig. 14.7 where both the plastic strain and excess free volume is plotted for several snapshots. Here it can be seen that the excess free volume accumulates ahead of the formation of the shear band.

The excess free volume model has also been used to study the transient response of deformation, specifically the stress overshoot common in homogeneous deformation at high temperatures as well as the suppression of free volume annihilation at low temperatures [45]. The excess free volume provides an opportunity to observe the evolution of the structure during deformation and provides unique insight in this mesoscale model.

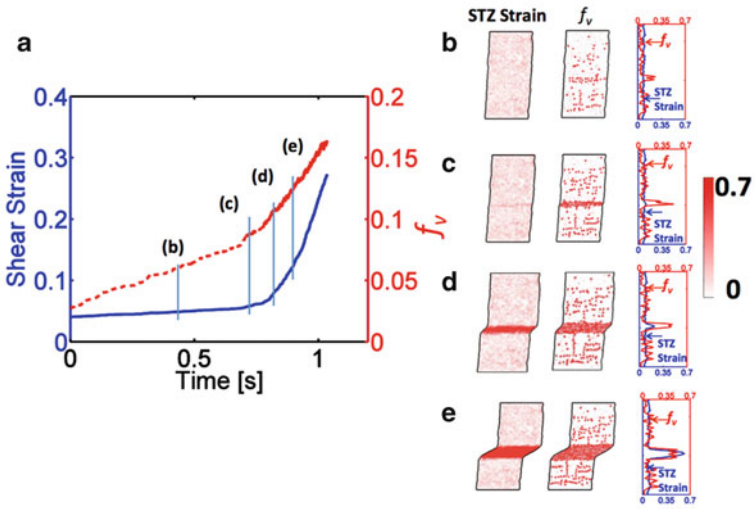

Fig. 14.7 (**a**) The shear strain and excess free volume f_v vs. time data of a cooled structure deformed at 300 K and 2 GPa shear load. (**b–e**) correspond to the snapshots at different times during the creep test. For each time, the physical deformation along with the magnitude of STZ strain and f_v are displayed; additionally, a plot with the 1D profile of STZ strain and f_v distributions along the vertical direction of the deformed sample is provided. Figure reproduced with permission from [55]

14.4.3 Correlations Between STZ Activations and Shear Banding

While a state variable such as free volume can capture the effects of processing or the evolution of the structure, we find that studying STZ behaviors in the absence of preexisting stress distributions also provides significant insight into the correlations between STZs.

Analysis of the 2D simulations discussed in Sect. 14.4.1 provides significant insight into correlations between STZ activations and the activation energy barrier distributions for the STZ activations [4]. Time-dependent radial distribution functions (TRDFs) can be constructed to show how STZ activations are correlated in both space and time. These TRDF functions indicate the likelihood of shearing an STZ at a nearby position and after a certain number of steps relative to a given STZ activation; magnitudes less than 1 are less likely to occur at a given position and time than if it occurred randomly throughout the simulation cell, and magnitudes greater than 1 are more likely to occur at a given position and time than if it occurred randomly throughout the simulation cell.

Representative TRDFs for low temperature, high stress and high temperature, high stress simulations are shown in Fig. 14.8. As can be seen in the figure, the low temperature, high stress conditions correspond to the preference for nearest-neighbor activations that is a maximum at the subsequent step and which decays over time. Despite the decay, however, there remains a preference to activate nearest-neighbor STZs in the region long after a given STZ is activated. This correlated behavior is the source for the shear localization that underlies the macroscopic shear bands that can be observed in experiments. Under conditions of high temperature, high stress it can be seen that there is no noticeable correlation between STZ activations. In other words, the additional thermal energy cancels the effect of stress concentrations that might otherwise cause shear localization. As a result, the STZ activations are uncorrelated, leading to uniform, random activation throughout the simulation cell causing homogeneous deformation. These distributions are representative of simulations that exhibited inhomogeneous and homogeneous deformation in Fig. 14.6a, across the range of conditions studied.

In addition to the ability to study correlations between STZ activations, one can study the formation of a shear band in detail [56]. Snapshots of a simulation cell subjected to a constant strain rate, uniaxial tension test are shown in Fig. 14.9. Analysis of the simulation indicates five different stages: (I) purely elastic, with no STZ activity, (II) STZ clustering, where correlated STZ activations lead to the formation of clusters, (III) growth following nucleation of a shear band, where all STZ activity transitions from being distributed throughout the simulation cell to being concentrated in the shear band, (IV) relaxation thickening, which is manifest by the continued thickening of the shear band while the stress is still dropping even after it has propagated across the simulation cell, and (V) flow thickening, which is indicated by the continued thickening of a single shear band at a constant flow stress. Most of the plastic strain is accumulated during prolonged flow thickening,

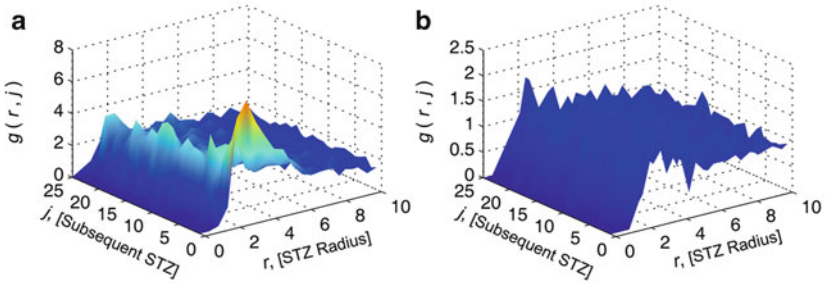

Fig. 14.8 TRDFs of STZ activation, where the behaviors and their corresponding conditions are (**a**) nearest-neighbor STZ activation: high stress and low temperature, and (**b**) independent STZ activation: high stress and high temperature. The shading of all the surfaces uses the same color scheme, permitting comparison of the magnitudes of the different trends. Figure reproduced with permission from [4]

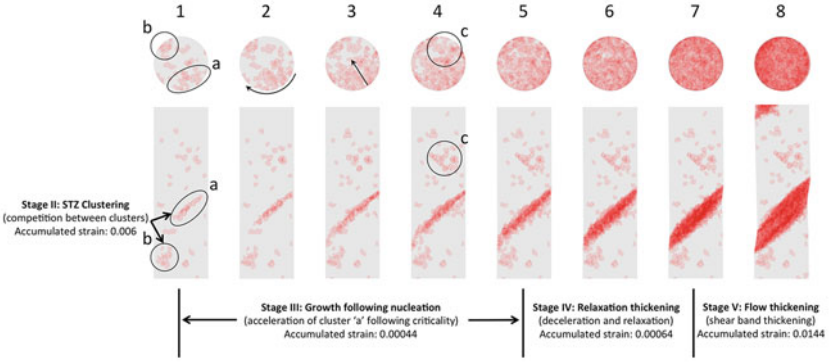

Fig. 14.9 Numbered snapshots of a model metallic glass at various times during a constant strain-rate, uniaxial tensile simulation. Each snapshot includes a semitransparent top and side view of the simulation cell. The evolution of the shear band is divided into four different stages following the initial elastic response. The shear band initiates at one of multiple potential nucleation sites formed during stage II. Once it achieves a critical state it exhibits a propagating shear front as it crosses the sample during stage III. The front propagation is followed by thickening of the shear band in stages IV and V, of which the majority of strain is accumulated during stage V. Figure reproduced with permission from [56]

indicating that nucleation and initial propagation of a shear band are very brief. The yield point matches a thermodynamic model for nucleation, and the work supports evidence that once a shear band nucleates, there is very little that can be done to stop it.

These types of studies demonstrate the strength of mesoscale models in elucidating the nanomechanics behind macroscopic processes. Some of these nanomechanical phenomena would be difficult to observe by other techniques.

14.4.4 Comparison with Experiments

Metallic glasses exhibit a broad range of interesting phenomena, one of which is that they can exhibit nanoscale strengthening when they are cyclically loaded in the elastic regime. This has been demonstrated in nanoindentation experiments where a metallic glass subjected to elastic cycling, which would otherwise leave behind no visible plastic deformation, shows a statistical increase in strength as a result of the cycling [59]. Interestingly, the cyclic strengthening can only occur if the cycling is of a sufficient magnitude, if the indenter is actually cycled (holding a constant load of equal magnitude and time does not lead to strengthening), and the strengthening saturates (one cannot cycle indefinitely to increase strength).

Since the cyclic loading is in the elastic regime, no structural changes can be detected during the cycling. Thus, modeling is an ideal method to elucidate the nanomechanics that cause the strengthening. The STZ dynamics framework is adapted to include contact mechanics in the finite element analysis solver and the modified-kMC algorithm is implemented due to the fact that the stress varies significantly as the indentation load is increased from zero to the point of plastic deformation [40].

Results from a simulation with monotonic loading are illustrated in Fig. 14.10. The deviation from the purely elastic solution can be observed, as well as the fact that a large region of the material exceeds the model yield point prior to the activation of any STZs, which is consistent with theory [46]. The STZs form slip lines early on but no distinct shear bands.

When subjected to cycling at different depths, the simulations indicate that significant plasticity can occur under the indented region without being evident in the load–displacement curve, the cyclic action leads to progressive STZ activity, although there is an indication for saturation of that activity. In other words, the simulations indicate that the energetics and time scales of STZ activity are plausible as a mechanism to cause structural evolution that would be consistent with nanoscale strengthening.

The nanoindentation simulation technique has also been used to detect the cause of the fluctuations in strength values for a metallic glass, which are reported as nanoscale strength distributions (NSDs) [57]. For example, in crystalline metals, the well-ordered structure leads to very specific energetic values to initiate plasticity and thermal excitations account for the fluctuations in the NSD. Amorphous metals on the other hand have larger fluctuations in strength and they do not have well-ordered structure, so any fluctuations could be due to structure or to thermal excitation. To help answer this question, simulated nanoindentation using the STZ dynamics framework is carried out on a model glass with a preexisting distribution of stress and strain but with no excess free volume state variable. The model is indented at the same position 10 times with different random number seeds to simulate thermal fluctuations. The same model is also indented at ten different locations (where the preexisting stress and strains are different) to simulate structural fluctuations. Figure 14.11 shows the NSDs as a function of the normalized load at the first

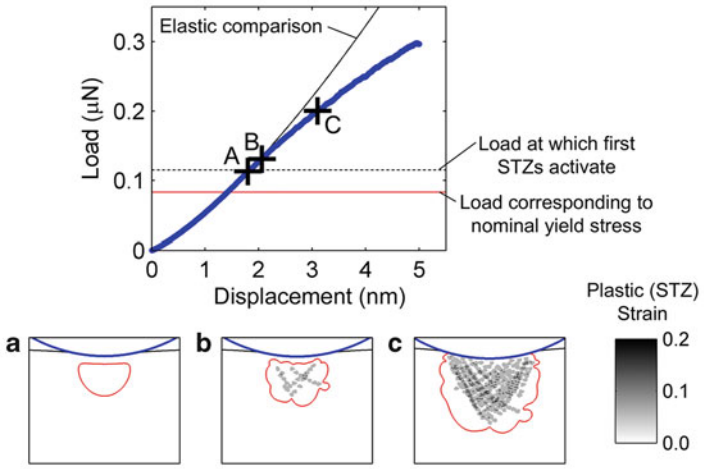

Fig. 14.10 Simulated nanoindentation results for monotonic loading. The graph shows the load–displacement curve for a single monotonic indentation test, with results for a purely elastic contact for comparison. Snapshots of the system during the simulation are provided below the graph as marked by "A," "B," and "C." The *red contour* on the snapshots shows the region of material that has exceeded the model yield stress, while the *gray* regions denote the operation of STZs. Figure reproduced with permission from [40]

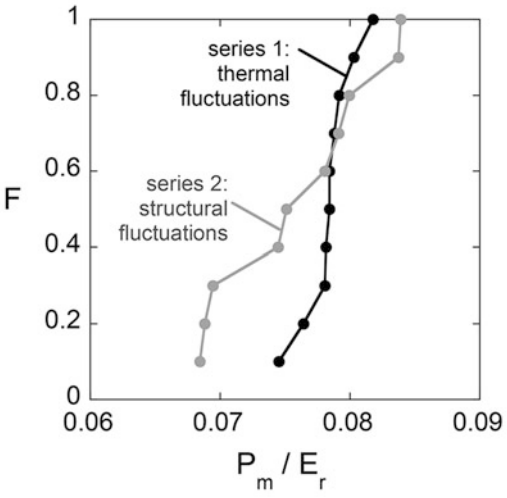

Fig. 14.11 Nanoscale strength distributions (NSDs) for the glass simulated by STZ dynamics. Here the first plasticity is measured as the point of the first STZ activation for two sets of simulations with different fluctuations imposed. For series 1, only thermal fluctuations are different among the tests in the series, while for series 2, the structure under the indenter was different in each of the ten cases. Figure reproduced with permission from [57]

STZ activation. Here it can be seen that the structural fluctuations cause more variation in load than the thermal fluctuations. In fact, the magnitude of the structural fluctuations matches well with the experimental variation in load, indicating that the structural fluctuations are the dominant source of variability in amorphous NSDs.

This application of a mesoscale technique to investigate the nanomechanics of experiments indicates the strong potential to elucidate phenomena that are difficult to measure by experimental techniques.

14.4.5 Composites

Due to the limited ductility in bulk metallic glasses, MGM composites have emerged as an attractive solution that retains most of the strength while providing significant ductility. These MGM composites can be created either by crystallizing regions of the material or by introducing a second phase during processing. The result is a metallic glass matrix that surrounds crystalline inclusions.

Research has demonstrated that the length scales, volume fraction, and ductility of the composite influence strength and ductility [47–54]. However, the exact relationships between the various microstructural factors and the material properties are not well understood.

The STZ dynamics framework can be adapted to allow two material models to be simulated [58], just as discussed in Sect. 14.3.4. This is accomplished by partitioning the mesh into the various phases and then directing the finite element analysis solver to use the appropriate material model for the phase of a given finite element. The STZ dynamics model is used for the amorphous matrix, while an isotropic hardening metal plasticity model is used for the crystalline inclusions. The kMC algorithm controls the time evolution of the system, though the metal plasticity model is not time dependent.

An n-factorial design of experiments is used to study three factors that are known to influence MGM composites: volume fraction of the crystalline phase, inclusion size of the crystalline phase, and yield point of the crystalline phase relative to the yield point of the amorphous matrix. High, low, and intermediate values of the three factors are studied, and simulation examples from the high and low values are provided in Fig. 14.12.

In Fig. 14.12 it can be seen that some combinations of the factors lead to improved plasticity while others lead to improved strength. Explicit, statistically significant functional forms for various dependent quantities, such as ductility, yield point, etc., can be extracted from the design of experiments. The functional forms of these dependent variables are in line with general expectations but demonstrate that increased volume fraction of a second phase alone is insufficient to improve ductility. The actual yield point of the second phase is critical to delocalizing the strain and improving ductility. These functional forms can even be used in the design and optimization of future MGM composites. The work also indicates different ways by which the crystalline inclusions delocalize the strain.

This simple adaptation of the STZ dynamics framework to more complex composites demonstrates the utility of a mesoscale framework to capture phenomena of multiphase materials while retaining the necessary view of the nanomechanics that control the behavior.

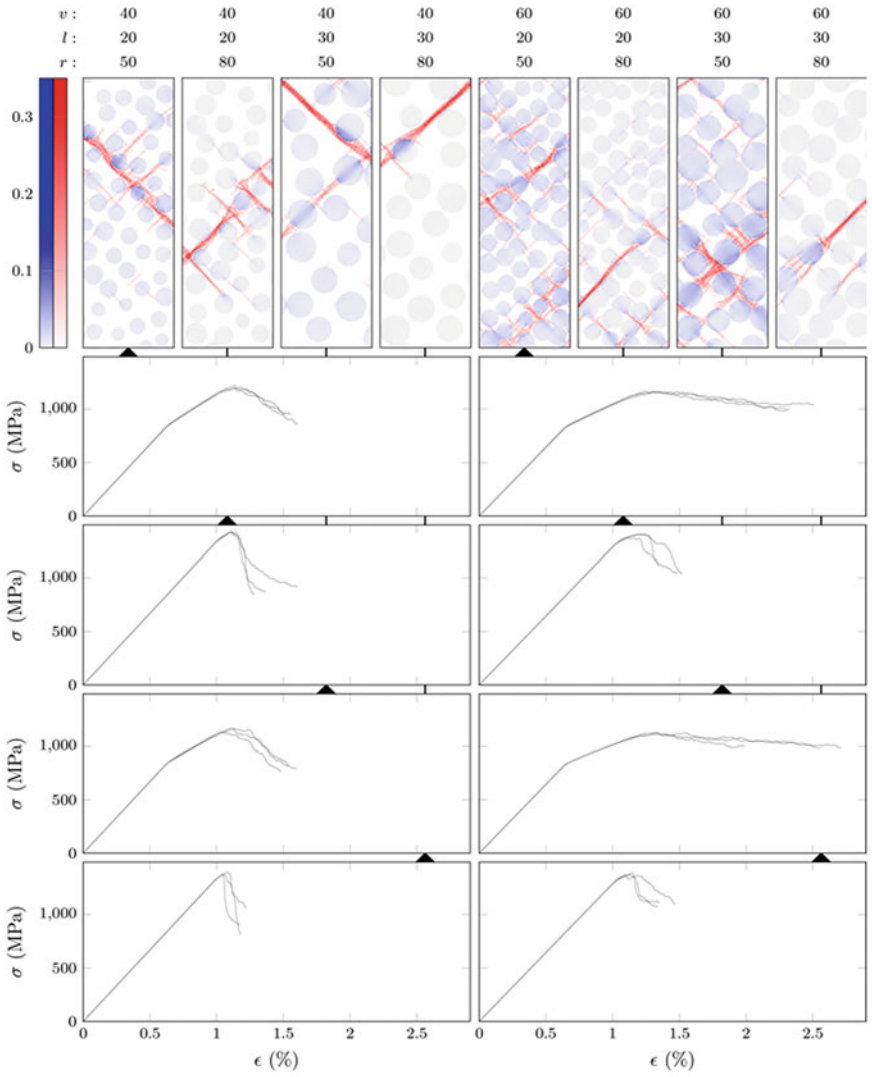

Fig. 14.12 Snapshots of the plastic strain in representative MGM composite simulations for different combinations of microstructural factors are shown. The microstructural factors and their values are v volume fraction of the crystalline phase at 40 and 60 %, l length scale of the crystalline inclusions at diameters of 20 and 30 nm, and r ratio of the crystalline yield point relative to the glass yield point at values of 50 and 80 %. The snapshots show crystalline inclusions in *gray*, glass plasticity in *red*, and crystalline plasticity in *blue*. Stress–strain curves are shown below each treatment to show the model response and the variability due to replicate simulations. Figure reproduced with permission from [58]

14.5 Conclusions

The combination of the kMC algorithm and a coarse-grained approach provides a useful framework with which to investigate the nanomechanical behavior of amorphous systems. The coarse-graining enables collections of atoms, or STZs, to be tracked rather than individual atoms and the kMC algorithm allows the shearing of these STZs to be controlled by stochastic processes based on the energetics of the system. The combination of these two features enables access to the relevant time and length scales while preserving a microscopic view of the processes that dominate the nanomechanical behavior.

As a result of the adaptability of the STZ dynamics framework, it has been used to investigate amorphous metal behavior in a variety of conditions. The modeling technique captures the overall deformation behaviors expected of a metallic glass. The technique also provides insight into the correlations between STZs and their formation into shear bands. The technique enables the study of the structural evolution and processing history to be readily accessed via a free volume state variable. Insight into nanoindentation experiments is possible through contact mechanics adaptations of the technique. MGM composites can be modeled through the combination of multiple materials models. It is expected that the STZ dynamics framework will continue to be useful in the investigation of amorphous metal behavior. In addition, the commonalities in deformation mechanics with other amorphous systems provide opportunities to study their behaviors as well.

Finally, the combination of the kMC algorithm with coarse-graining techniques has a wide range of possible applications outside amorphous systems or deformation nanomechanics. These mesoscale modeling techniques can be applied in myriad ways.

References

1. C.A. Schuh, T.C. Hufnagel, U. Ramamurty, Mechanical behavior of amorphous alloys. Acta Mater. **55**, 4067–4109 (2007)
2. D. Rodney, A. Tanguy, D. Vandembroucq, Modeling the mechanics of amorphous solids at different length scale and time scale. Model. Simul. Mater. Sci. Eng. **19**, 083001 (2011)
3. A.S. Argon, Plastic deformation in metallic glasses. Acta Metall. Mater. **27**, 47–58 (1979)
4. E.R. Homer, D. Rodney, C.A. Schuh, Kinetic Monte Carlo study of activated states and correlated shear-transformation-zone activity during the deformation of an amorphous metal. Phys. Rev. B. **81**, 064204 (2010)
5. A. Tanguy, F. Leonforte, J.-L. Barrat, Plastic response of a 2D Lennard-Jones amorphous solid: detailed analysis of the local rearrangements at very slow strain rate. Eur. Phys. J. E. **20**, 355–364 (2006)
6. C.E. Maloney, A. Lemaitre, Amorphous systems in athermal, quasistatic shear. Phys. Rev. E **74**, 016118 (2006)
7. F. Abdeljawad, M. Haataja, Continuum modeling of bulk metallic glasses and composites. Phys. Rev. Lett. **105**, 125503 (2010)

8. L. Anand, C. Su, A constitutive theory for metallic glasses at high homologous temperatures. Acta Mater. **55**, 3735–3747 (2007)
9. L. Anand, C. Su, A theory for amorphous viscoplastic materials undergoing finite deformations, with application to metallic glasses. J. Mech. Phys. Solids **53**, 1362–1396 (2005)
10. C. Su, L. Anand, Plane strain indentation of a Zr-based metallic glass: experiments and numerical simulation. Acta Mater. **54**, 179–189 (2006)
11. S. Yip, M.P. Short, Multiscale materials modelling at the mesoscale. Nat. Mater. **12**, 774–777 (2013)
12. S. Yip (ed.), *Handbook of Materials Modeling* (Springer, Dordrecht, 2005)
13. A.F. Voter, Introduction to the kinetic Monte Carlo method, in *Radiation Effects in Solids*, ed. by K.E. Sickafus, E.A. Kotomin, B.P. Uberuaga (Springer, Dordrecht, 2007), pp. 1–23
14. E.R. Homer, C.A. Schuh, Mesoscale modeling of amorphous metals by shear transformation zone dynamics. Acta Mater. **57**, 2823–2833 (2009)
15. C. Domain, C.S. Becquart, L. Malerba, Simulation of radiation damage in Fe alloys: an object kinetic Monte Carlo approach. J. Nucl. Mater. **335**, 121–145 (2004)
16. C.S. Deo, D.J. Srolovitz, W. Cai, V.V. Bulatov, Kinetic Monte Carlo method for dislocation migration in the presence of solute. Phys. Rev. B **71**, 014106 (2005)
17. F. Roters, P. Eisenlohr, L. Hantcherli, D.D. Tjahjanto, T.R. Bieler, D. Raabe, Overview of constitutive laws, kinematics, homogenization and multiscale methods in crystal plasticity finite-element modeling: theory, experiments, applications. Acta Mater. **58**, 1152–1211 (2010)
18. Y. Mishin, M. Asta, J. Li, Atomistic modeling of interfaces and their impact on microstructure and properties. Acta Mater. **58**, 1117–1151 (2010)
19. R. Devanathan, L. Van Brutzel, A. Chartier, C. Gueneau, A.E. Mattsson, V. Tikare, T. Bartel, T. Besmann, M. Stan, P. Van Uffelen, Modeling and simulation of nuclear fuel materials. Energy Environ. Sci. **3**, 1406–1426 (2010)
20. P. Zhao, J. Li, Y. Wang, Heterogeneously randomized STZ model of metallic glasses: softening and extreme value statistics during deformation. Int J Plast **40**, 1–22 (2013)
21. Y. Chen, C.A. Schuh, A coupled kinetic Monte Carlo–finite element mesoscale model for thermoelastic martensitic phase transformations in shape memory alloys. Acta Mater. **83**, 431–447 (2015)
22. D. Frenkel, B. Smit, *Understanding Molecular Simulation* (Academic, San Diego, 2002)
23. V.V. Bulatov, A.S. Argon, A stochastic model for continuum elasto-plastic behavior: I. Numerical approach and strain localization. Model. Simul. Mater. Sci. Eng. **2**, 167–184 (1994)
24. V.V. Bulatov, A.S. Argon, A stochastic model for continuum elasto-plastic behavior: II. A study of the glass-transition and structural relaxation. Model. Simul. Mater. Sci. Eng. **2**, 185–202 (1994)
25. V.V. Bulatov, A.S. Argon, A stochastic model for continuum elasto-plastic behavior: III. Plasticity in ordered versus disordered solids. Model. Simul. Mater. Sci. Eng. **2**, 203–222 (1994)
26. D.J. Srolovitz, V. Vitek, T. Egami, An atomistic study of deformation of amorphous metals. Acta Metall. Mater. **31**, 335–352 (1983)
27. C.E. Maloney, A. Lemaitre, Universal breakdown of elasticity at the onset of material failure. Phys. Rev. Lett. **93**, 195501 (2004)
28. D. Rodney, C.A. Schuh, Distribution of thermally activated plastic events in a flowing glass. Phys. Rev. Lett. **102**, 235503 (2009)
29. E.R. Homer, C.A. Schuh, Three-dimensional shear transformation zone dynamics model for amorphous metals. Model. Simul. Mater. Sci. Eng. **18**, 065009 (2010)
30. T. Mura, *Micromechanics of Defects in Solids* (Kluwer, Dordrecht, 1991)
31. T.W. Clyne, P.J. Withers, *An Introduction to Metal Matrix Composites* (Cambridge University Press, Cambridge, 1993)
32. E.B. Tadmor, R.E. Miller, *Modeling Materials* (Cambridge University Press, New York, 2011)
33. R. Malek, N. Mousseau, Dynamics of Lennard-Jones clusters: a characterization of the activation-relaxation technique. Phys. Rev. E **62**, 7723–7728 (2000)

34. E. Cancès, F. Legoll, M.C. Marinica, K. Minoukadeh, F. Willaime, Some improvements of the activation-relaxation technique method for finding transition pathways on potential energy surfaces. J. Chem. Phys. **130**, 114711 (2009)
35. D. Rodney, C.A. Schuh, Yield stress in metallic glasses: the jamming-unjamming transition studied through Monte Carlo simulations based on the activation-relaxation technique. Phys. Rev. B **80**, 184203 (2009)
36. W.L. Johnson, K. Samwer, A universal criterion for plastic yielding of metallic glasses with a $(T/Tg)^{2/3}$ temperature dependence. Phys. Rev. Lett. **95**, 195501 (2005)
37. W.H. Wang, P. Wen, D.Q. Zhao, M.X. Pan, R.J. Wang, Relationship between glass transition temperature and Debye temperature in bulk metallic glasses. J. Mater. Res. **18**, 2747–2751 (2003)
38. M. Zink, K. Samwer, W.L. Johnson, S.G. Mayr, Plastic deformation of metallic glasses: size of shear transformation zones from molecular dynamics simulations. Phys. Rev. B **73**, 172203 (2006)
39. X.L. Fu, Y. Li, C.A. Schuh, Homogeneous flow of bulk metallic glass composites with a high volume fraction of reinforcement. J. Mater. Res. **22**, 1564–1573 (2007)
40. C.E. Packard, E.R. Homer, N. Al-Aqeeli, C.A. Schuh, Cyclic hardening of metallic glasses under Hertzian contacts: experiments and STZ dynamics simulations. Philos. Mag. **90**, 1373–1390 (2010)
41. Y. Shi, M.L. Falk, Stress-induced structural transformation and shear banding during simulated nanoindentation of a metallic glass. Acta Mater. **55**, 4317–4324 (2007)
42. M.L. Falk, Molecular-dynamics study of ductile and brittle fracture in model noncrystalline solids. Phys. Rev. B **60**, 7062–7070 (1999)
43. F. Spaepen, Homogeneous flow of metallic glasses: a free volume perspective. Scr. Mater. **54**, 363–367 (2006)
44. T. Egami, Formation and deformation of metallic glasses: atomistic theory. Intermetallics **14**, 882–887 (2006)
45. L. Li, N. Wang, F. Yan, Transient response in metallic glass deformation: a study based on shear transformation zone dynamics simulations. Scr. Mater. **80**, 25–28 (2014)
46. C.E. Packard, C.A. Schuh, Initiation of shear bands near a stress concentration in metallic glass. Acta Mater. **55**, 5348–5358 (2007)
47. A.C. Lund, C.A. Schuh, Critical length scales for the deformation of amorphous metals containing nanocrystals. Philos. Mag. Lett. **87**, 603–611 (2007)
48. Y. Wang, J. Li, A.V. Hamza, T.W. Barbee, Ductile crystalline-amorphous nanolaminates. Proc. Natl. Acad. Sci. U. S. A. **104**, 11155–11160 (2007)
49. X.L. Fu, Y. Li, C.A. Schuh, Mechanical properties of metallic glass matrix composites: effects of reinforcement character and connectivity. Scr. Mater. **56**, 617–620 (2007)
50. T.G. Nieh, J. Wadsworth, Bypassing shear band nucleation and ductilization of an amorphous-crystalline nanolaminate in tension. Intermetallics **16**, 1156–1159 (2008)
51. D.C. Hofmann, J.-Y. Suh, A. Wiest, G. Duan, M.-L. Lind, M.D. Demetriou, W.L. Johnson, Designing metallic glass matrix composites with high toughness and tensile ductility. Nature **451**, 1085–1089 (2008)
52. S. Scudino, B. Jerliu, S. Pauly, K.B. Surreddi, U. Kühn, J. Eckert, Ductile bulk metallic glasses produced through designed heterogeneities. Scr. Mater. **65**, 815–818 (2011)
53. Y.S. Oh, C.P. Kim, S. Lee, N.J. Kim, Microstructure and tensile properties of high-strength high-ductility Ti-based amorphous matrix composites containing ductile dendrites. Acta Mater. **59**, 7277–7286 (2011)
54. R.T. Qu, J.X. Zhao, M. Stoica, J. Eckert, Z.F. Zhang, Macroscopic tensile plasticity of bulk metallic glass through designed artificial defects. Mater. Sci. Eng. A **534**, 365–373 (2012)
55. L. Li, E.R. Homer, C.A. Schuh, Shear transformation zone dynamics model for metallic glasses incorporating free volume as a state variable. Acta Mater. **61**, 3347–3359 (2013)
56. E.R. Homer, Examining the initial stages of shear localization in amorphous metals. Acta Mater. **63**, 44–53 (2014)

57. C.E. Packard, O. Franke, E.R. Homer, C.A. Schuh, Nanoscale strength distribution in amorphous versus crystalline metals. J. Mater. Res. **25**, 2251–2263 (2010)
58. T.J. Hardin, E.R. Homer, Microstructural factors of strain delocalization in model metallic glass matrix composites. Acta Mater. **83**, 203–215 (2015)
59. C.E. Packard, L.M. Witmer, C.A. Schuh, Hardening of a metallic glass during cyclic loading in the elastic range, Appl Phys Letters. **92**, (2008) 171911. doi:10.1063/1.2919722.